

Scaling of Magnetic Dissipation and Particle Acceleration in ABC Fields

Qiang Chen^{1†}, Krzysztof Nalewajko¹, Bhupendra Mishra²

¹Nicolaus Copernicus Astronomical Center, Polish Academy of Sciences, Bartycka 18, 00-716 Warsaw, Poland

²Los Alamos National Laboratory, Los Alamos, NM 87545, USA

(Received 5 October 2020; revised 9 January 2021; accepted 5 February 2021)

Using particle-in-cell (PIC) numerical simulations with electron-positron pair plasma, we study how the efficiencies of magnetic dissipation and particle acceleration scale with the initial coherence length λ_0 in relation to the system size L of the two-dimensional (2D) ‘Arnold-Beltrami-Childress’ (ABC) magnetic field configurations. Topological constraints on the distribution of magnetic helicity in 2D systems, identified earlier in relativistic force-free (FF) simulations, that prevent the high- (L/λ_0) configurations from reaching the Taylor state, limit the magnetic dissipation efficiency to about $\epsilon_{\text{diss}} \simeq 60\%$. We find that the peak growth time scale of the electric energy $\tau_{\text{E,peak}}$ scales with the characteristic value of initial Alfvén velocity $\beta_{\text{A,ini}}$ like $\tau_{\text{E,peak}} \propto (\lambda_0/L)\beta_{\text{A,ini}}^{-3}$. The particle energy change is decomposed into non-thermal and thermal parts, with non-thermal energy gain dominant only for high initial magnetisation. The most robust description of the non-thermal high-energy part of the particle distribution is that the power-law index is a linear function of the initial magnetic energy fraction.

Key words: plasma instabilities, plasma simulation, astrophysical plasmas

1. Introduction

Certain high-energy astrophysical sources are characterised by luminous and rapid flares of energetic radiation. In particular, these include blazars (e.g., Aharonian *et al.* 2007; Albert *et al.* 2007; Aleksić *et al.* 2011; Abdo *et al.* 2011*b*; Nalewajko 2013; Ackermann *et al.* 2016), and the Crab pulsar wind nebula (Tavani *et al.* 2011; Abdo *et al.* 2011*a*; Buehler *et al.* 2012; Lyubarsky 2012; Mayer *et al.* 2013; Striani *et al.* 2013). In these extreme astrophysical environments, magnetic fields may dominate even the local rest-mass energy density. Magnetic reconnection is considered a leading explanation for the efficient particle acceleration behind the dramatic gamma-ray flares of blazars (Giannios *et al.* 2009; Nalewajko *et al.* 2011, 2012; Giannios 2013; Sironi *et al.* 2015; Petropoulou *et al.* 2016). Through changes of the magnetic line topology, particles are accelerated in the current sheets, converting magnetic energy into kinetic and thermal energy. In the case of the Crab pulsar wind nebula, the γ -ray radiation spectral peaks can surpass the classical synchrotron radiation reaction limit (~ 160 MeV), which suggests a very efficient localised dissipation of magnetic energy that allows for rapid particle acceleration (Uzdensky *et al.* 2011; Komissarov & Lyutikov 2011; Arons 2012; Clausen-

† Email address for correspondence: chen@camk.edu.pl

Brown & Lyutikov 2012; Komissarov 2012; Buehler & Blandford 2014; Zrake 2016; Zrake & Arons 2017; Lyutikov *et al.* 2018).

Numerical simulations based on the kinetic particle-in-cell (PIC) algorithm have demonstrated that relativistic reconnection in collisionless plasma is an efficient mechanism of magnetic energy dissipation and particle acceleration (Zenitani & Hoshino 2001; Jaroschek *et al.* 2004; Zenitani & Hoshino 2007; Lyubarsky & Liverts 2008; Liu *et al.* 2011; Bessho & Bhattacharjee 2012; Kagan *et al.* 2013; Sironi & Spitkovsky 2014; Guo *et al.* 2014; Melzani, Mickaël *et al.* 2014; Guo *et al.* 2015, 2016; Werner *et al.* 2016; Werner & Uzdensky 2017; Werner *et al.* 2018; Petropoulou & Sironi 2018; Petropoulou *et al.* 2019; Guo *et al.* 2019, 2020), and that it can produce extreme radiative signatures — energetic, highly anisotropic and rapidly variable (Cerutti *et al.* 2012, 2013, 2014; Kagan *et al.* 2016; Nalewajko 2018; Christie *et al.* 2018; Mehlhaff *et al.* 2020; Comisso *et al.* 2020; Ortuño-Macías & Nalewajko 2020). Most of these simulations were initiated from relativistic Harris-type current layers (Kirk & Skjaraasen 2003).

An alternative class of magnetostatic equilibria known as the ‘Arnold-Beltrami-Childress’ (ABC) magnetic fields (Arnold 1965) has been recently applied as an initial configuration for investigating relativistic magnetic dissipation (East *et al.* 2015). This configuration involves no kinetically thin current sheets, but is unstable to the so-called coalescence modes that lead to localised interactions of magnetic domains of opposite polarities, emergence of dynamical current layers, instantaneous particle acceleration, and production of rapid flares of high-energy radiation. The overall process has been dubbed *magnetoluminescence* – a generic term for efficient and fast conversion of magnetic energy into radiation (Blandford *et al.* 2017).

Numerical simulations of ABC fields have been performed with relativistic magnetohydrodynamics (MHD) and relativistic force-free (FF) algorithms (East *et al.* 2015). Detailed comparison between 2D and 3D ABC fields in the FF framework has been performed by Zrake & East (2016). PIC simulations of 2D ABC fields have been reported by Nalewajko *et al.* (2016) with the focus on the structure of current layers and particle acceleration, by Yuan *et al.* (2016) including synchrotron radiation reaction and radiative signatures, and by Nalewajko *et al.* (2018) including synchrotron and Inverse Compton (IC) radiation. ABC fields have been also investigated in great detail (including PIC simulations) by Lyutikov *et al.* (2017*a,b*, 2018) with application to the Crab Nebula flares. The first three-dimensional PIC simulations of ABC fields have been reported in Nalewajko (2018).

The previous works have established the following picture. ABC fields simulated in periodic numerical grids are unstable to coalescence instability if only there exists a state of equal total magnetic helicity and lower total magnetic energy (East *et al.* 2015). The growth time scale of the linear coalescence instability is a fraction of the light crossing time scale that depends on the mean magnetisation (or equivalently on the typical Alfvén velocity) (Nalewajko *et al.* 2016). The magnetic dissipation efficiency is determined primarily by the global magnetic field topology, and it is restricted in 2D systems due to the existence of additional topological invariants (Zrake & East 2016). The dissipated magnetic energy is transferred to the particles, resulting in non-thermal high-energy tails of their energy distributions. These tails can be in most cases described as power laws with a power-law index, but more generally they can be characterised by the non-thermal number and energy fractions (Nalewajko *et al.* 2016). With increasing initial magnetisation, the non-thermal tails become harder, containing higher number and energy fractions, similar to the results on Harris-layer reconnection Sironi & Spitkovsky (2014); Guo *et al.* (2014); Werner *et al.* (2016). A limitation of the ABC fields in

comparison with the Harris layers is that the initial magnetisation is limited for a given simulation size by the minimum particle densities required to sustain volumetric currents.

The particle acceleration mechanisms of ABC fields, described in more detail in Nalewajko *et al.* (2016); Yuan *et al.* (2016); Lyutikov *et al.* (2017a), show similarities to other numerical approaches to the problem of relativistic magnetic dissipation. During the linear stage of coalescence instability, kinetically thin current layers form and evolve very dynamically. The few particles that happen to straggle into one of those layers are accelerated by direct non-ideal reconnection electric fields ($\mathbf{E} \cdot \mathbf{B} \neq 0$, $|\mathbf{E}| > |\mathbf{B}|$). This is essentially the Zenitani & Hoshino (2001) picture of magnetic X-point, which is important also in large-scale simulations of Harris-layer reconnection in the sense that particles that pass through a magnetic X-point are most likely to eventually reach top energies (Sironi & Spitkovsky 2014; Guo *et al.* 2019). The non-linear stage of coalescence instability features slowly damped electric oscillations that gradually convert to particle energies. This can affect essentially all particles, as electric oscillations cross the entire simulation volume multiple times. Particles accelerated during the linear stage now propagate on wide orbits and can interact with electric perturbations at random angles. This is reminiscent of a Fermi process, in particular of the kind envisioned by Hoshino (2012). With a larger number of magnetic domains, the coalescence proceeds in multiple stages, with the successive current layers increasingly less regular. The system becomes chaotic more quickly and begins to resemble a decaying turbulence of the kind studied by Comisso & Sironi (2019).

As the previous PIC simulations of ABC fields were largely limited to the lowest unstable mode, in this work we present the results of new series of 2D PIC simulations of ABC fields for different coherence lengths λ_0 in order to understand how they affect the efficiency of magnetic dissipation and particle acceleration. Although the coalescence instability is rather fast, it is followed by slowly damped non-linear oscillations, hence our simulations are run for at least $25L/c$ light crossing times for the system size L to allow these oscillations to settle. Our simulations were performed at three different sizes, in addition we investigated the effects of numerical resolution and local particle anisotropy, in order to break the relation between the effective wavenumber and the mean initial magnetisation. We also compare our results with new 3D simulations following the setup described in Nalewajko (2018).

In Section 2 we define the initial configuration of our simulations. Our results are presented in Section 3, including spatial distributions of magnetic fields (Section 3.1), evolution of the total energy components (Section 3.2), conservation accuracy of the magnetic helicity (Section 3.3), and particle energy distributions (Section 3.4). Discussion is provided in Section 4.

2. Simulation setup

We perform a series of PIC simulations using the `Zeltron` code[†] (Cerutti *et al.* 2013) of 2D periodic magnetic equilibria known as ABC fields (East *et al.* 2015). As opposed to the Harris layers, these initial configurations do not contain kinetically thin current layers. In 2D, there are two ways to implement ABC fields on a periodic grid, which we call diagonal or parallel, referring to the orientation of the separatrices between individual magnetic domains. The *diagonal* ABC field is defined as:

$$B_x(x, y) = B_0 \sin(2\pi y/\lambda_0), \quad (2.1)$$

[†] <http://benoit.cerutti.free.fr/Zeltron/>

$$B_y(x, y) = B_0 \cos(2\pi x/\lambda_0), \quad (2.2)$$

$$B_z(x, y) = B_0 [\sin(2\pi x/\lambda_0) + \cos(2\pi y/\lambda_0)], \quad (2.3)$$

where λ_0 is the coherence length. The *parallel* ABC field can be obtained from the diagonal one through rotation by 45° and increasing the effective wavenumber by factor $\sqrt{2}$:

$$B_x(x, y) = B_0 \left[\sin(\sqrt{2}\pi(x+y)/\lambda_0) + \sin(\sqrt{2}\pi(x-y)/\lambda_0) \right] / \sqrt{2}, \quad (2.4)$$

$$B_y(x, y) = B_0 \left[\sin(\sqrt{2}\pi(x-y)/\lambda_0) - \sin(\sqrt{2}\pi(x+y)/\lambda_0) \right] / \sqrt{2}, \quad (2.5)$$

$$B_z(x, y) = B_0 \left[\cos(\sqrt{2}\pi(x+y)/\lambda_0) - \cos(\sqrt{2}\pi(x-y)/\lambda_0) \right]. \quad (2.6)$$

With this, both the diagonal and parallel configurations satisfy the Beltrami condition $\nabla \times \mathbf{B} = -(2\pi/\lambda_0)\mathbf{B}$. In all cases, the mean squared magnetic field strength is $\langle B^2 \rangle = 2B_0^2$ and the maximum magnetic field strength is $B_{\max} = 2B_0$.

These magnetic fields are maintained in an initial equilibrium by volumetric current densities $\mathbf{j}(\mathbf{x}) = -(c/2\lambda_0)\mathbf{B}(\mathbf{x})$ provided by locally anisotropic particle distribution (for details, see Nalewajko *et al.* 2016; Nalewajko 2018). ABC fields are characterised by vanishing divergence of the electromagnetic stress tensor $\partial_i T_{EM}^{ij} = 0$ (equivalent to the vanishing $\mathbf{j} \times \mathbf{B}$ force), which implies uniform gas pressure that can be realised with uniform temperature T and uniform gas density n . We chose the initial particle energy distribution to be Maxwell-Jüttner distribution of relativistic temperature $\Theta = kT/mc^2 = 1$, hence the mean particle energy is $\langle \gamma \rangle \simeq 3.37$, and the mean particle velocity is $\langle \beta \rangle \simeq 0.906$. The gas density (including both the electrons and positrons) is given by:

$$n = \frac{3B_0}{2e\tilde{a}_1 \langle \beta \rangle \lambda_0} \quad (2.7)$$

where $\tilde{a}_1 \leq 1/2$ is a constant that normalises the dipole moment of the local particle distribution. We chose $\tilde{a}_1 = 1/4$ as a standard value, but we investigate the effect of reduced local particle anisotropy with lower values of \tilde{a}_1 that result in higher particle densities and lower magnetisation values. The initial kinetic energy density is:

$$u_{\text{kin,ini}} = \langle \gamma \rangle nm_e c^2 \simeq \frac{6\pi \langle \gamma \rangle}{\tilde{a}_1 \Theta \langle \beta \rangle} \left(\frac{\rho_0}{\lambda_0} \right) \langle u_{B,\text{ini}} \rangle, \quad (2.8)$$

where $\rho_0 = \Theta m_e c^2 / (eB_0)$ is the nominal gyroradius, and $\langle u_{B,\text{ini}} \rangle = B_0^2 / 4\pi$ is the initial mean magnetic energy density. The initial mean hot magnetisation is given by:

$$\langle \sigma_{\text{ini}} \rangle = \frac{\langle B^2 \rangle}{4\pi w} = \frac{\tilde{a}_1 \Theta \langle \beta \rangle}{3\pi(\langle \gamma \rangle + \Theta)} \left(\frac{\lambda_0}{\rho_0} \right), \quad (2.9)$$

where $w = (\langle \gamma \rangle + \Theta)nm_e c^2$ is the relativistic enthalpy density. For $\Theta = 1$, we have $\langle \sigma_{\text{ini}} \rangle \simeq (4\tilde{a}_1)(\lambda_0/182\rho_0)$.

We performed simulations of either diagonal or parallel ABC fields and for different wavenumbers k ($k = L/\lambda_0$ for diagonal configuration and $k = L/\sqrt{2}\lambda_0$ for parallel configuration). For instance, a simulation labelled `diag_k2` is initiated with a diagonal ABC field with $L/\lambda_0 = 2$. In order to verify the scaling of our results, we performed series of simulations for three sizes of numerical grids: small (s) for $N_x = N_y = 1728$, medium (m) for $N_x = N_y = 3456$, and large (l) $N_x = N_y = 6912$. For numerical resolution $\Delta x = \Delta y = L/N_x$, where L is the physical system size we chose a standard value of $\Delta x = \rho_0/2.4$, but we investigated the effect of increased resolution on the medium numerical grid. The numerical time step was chosen as $\Delta t = 0.99(\Delta x/\sqrt{2}c)$. All of our

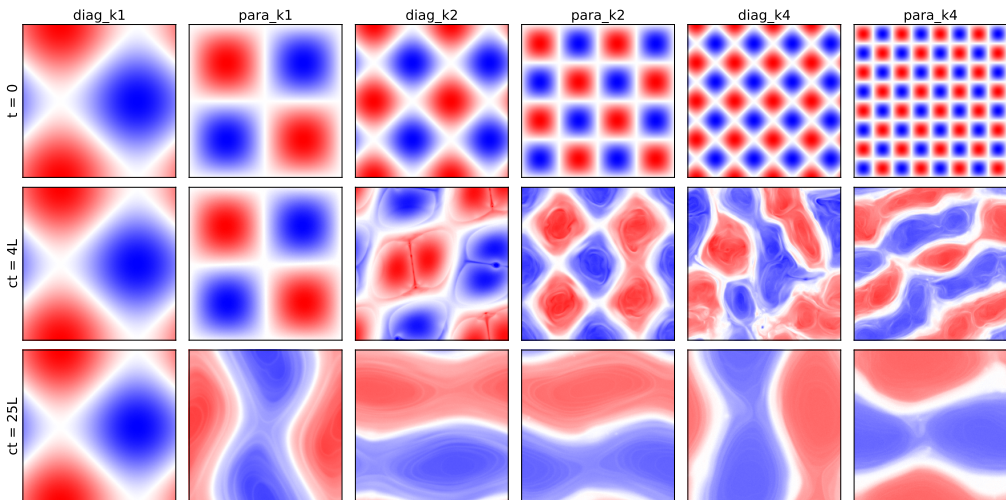


FIGURE 1. Spatial distributions of the out-of-plane magnetic field component B_z for ABC fields of different initial topologies. Each column of panels compares the initial configuration at $ct/L = 0$ (top) with an intermediate state at $ct/L \simeq 4$ (middle), and with the final state at $ct/L \simeq 25$ (bottom).

simulations were performed for at least $25L/c$ light crossing times. In each case we used 128 macroparticles (including both species) per cell.

We also performed two new 3D simulations for the cases **diag_k2** and **diag_k4**, following the configuration described in Nalewajko (2018), but extending them to $25L/c$. In this case we chose the following parameter values: $N_x = N_y = N_z = 1152$, $\Delta x = \Delta y = \Delta z = \rho_0/1.28$, $\tilde{a}_1 = 0.2$, and 16 macroparticles per cell.

3. Results

The key parameters of our large simulations are listed in Table 1, where we report basic results describing global energy transformations that will be discussed in Section 3.2, and particle energy distributions that will be discussed in Section 3.4.

3.1. Spatial distribution of magnetic fields

Fig. 1 compares the initial ($ct/L = 0$), intermediate ($ct/L \simeq 4$) and final ($ct/L \simeq 25$) configurations of the out-of-plane magnetic field component B_z . The initial configurations have the form of periodic grids of B_z minima (blue) and maxima (red). The case **diag_k1** is the only one that represents a stable equilibrium, as it involves only one minimum and one maximum of B_z . The case **para_k1** (investigated in detail in Nalewajko *et al.* 2016; Yuan *et al.* 2016) begins with two minima and two maxima of B_z , by $ct/L \simeq 4$ it is just entering the linear instability stage, and the final state appears very similar to the case **diag_k1**, although the domains of positive and negative B_z are still slightly perturbed. As we increase L/λ_0 , throughout the case of **para_k4**, the intermediate states become more evolved, at further stages of magnetic domains coalescence, while the final states in all cases consist of single positive and negative B_z domains. We notice that these domains become separated by increasingly broad bands of $B_z \simeq 0$.

TABLE 1. Global parameters of energy conversion and particle acceleration compared for the 2D and 3D simulations. The initial values denoted with subscript *ini* are measured at $t = 0$, and the final values (*fin*) are averaged over $20 \leq ct/L \leq 25$. The initial mean hot magnetisation $\langle \sigma_{ini} \rangle$ is computed from Eq. (2.9). The initial magnetic energies $\mathcal{E}_{B,ini}$ are normalised to the total system energy \mathcal{E}_{tot} . The magnetic dissipation efficiency is defined as $\epsilon_{diss} = 1 - \mathcal{E}_{B,fin}/\mathcal{E}_{B,ini}$. We report the peak value $\tau_{E,peak}$ of the linear growth time scale τ_E of electric energy, which scales like $\mathcal{E}_E \propto \exp(ct/L\tau_E)$. For the final particle energy distributions, we report: the power law index p , the maximum Lorentz factor γ_{max} , and the non-thermal particle energy fraction f_E .

config	$\frac{L}{\lambda_0}$	\tilde{a}_1	$\frac{\rho_0}{\Delta x}$	$\langle \sigma_{ini} \rangle$	$\mathcal{E}_{B,ini}$	$\epsilon_{diss,fin}$	$\tau_{E,peak}$	p	γ_{max}	f_E
2D small, $N_x = 1728$										
para_k1	$\sqrt{2}$	1/4	2.4	2.8	0.65	0.26	0.25	3.1	450	0.18
para_k2	$2\sqrt{2}$	1/4	2.4	1.4	0.48	0.52	0.17	3.75	190	0.16
para_k4	$4\sqrt{2}$	1/4	2.4	0.7	0.31	0.59	0.14	4.8	60	0.07
para_k8	$8\sqrt{2}$	1/4	2.4	0.4	0.19	0.65	0.17	—	30	0.02
2D medium, $N_x = 3456$										
para_k1	$\sqrt{2}$	1/4	2.4	5.6	0.78	0.27	0.21	2.85	870	0.31
diag_k2	2	1/4	2.4	4.0	0.72	0.44	0.16	2.95	620	0.34
para_k2	$2\sqrt{2}$	1/4	2.4	2.8	0.65	0.53	0.13	3.2	590	0.28
diag_k4	4	1/4	2.4	2.0	0.56	0.57	0.11	3.65	270	0.20
para_k4	$4\sqrt{2}$	1/4	2.4	1.4	0.48	0.59	0.09	3.8	190	0.15
diag_k8	8	1/4	2.4	1.0	0.39	0.60	0.08	4.2	100	0.10
para_k8	$8\sqrt{2}$	1/4	2.4	0.7	0.31	0.61	0.08	4.8	60	0.06
para_k1	$\sqrt{2}$	1/8	2.4	2.8	0.64	0.26	0.27	3.35	320	0.18
para_k1	$\sqrt{2}$	1/16	2.4	1.4	0.48	0.26	0.40	4.5	80	0.07
para_k1	$\sqrt{2}$	1/32	2.4	0.7	0.31	0.25	0.68	—	30	0.02
para_k2	$2\sqrt{2}$	1/8	2.4	1.4	0.48	0.51	0.19	4.2	150	0.13
para_k2	$2\sqrt{2}$	1/16	2.4	0.7	0.31	0.48	0.34	—	50	0.04
para_k4	$4\sqrt{2}$	1/8	2.4	0.7	0.31	0.57	0.17	5.2	60	0.05
para_k4	$4\sqrt{2}$	1/16	2.4	0.4	0.19	0.54	0.46	—	30	0.01
para_k8	$8\sqrt{2}$	1/8	2.4	0.4	0.19	0.58	0.20	—	30	0.01
para_k1	$\sqrt{2}$	1/4	4.8	2.8	0.64	0.26	0.25	3.2	410	0.18
para_k1	$\sqrt{2}$	1/4	9.6	1.4	0.48	0.26	0.32	3.8	160	0.10
para_k1	$\sqrt{2}$	1/4	19.2	0.7	0.31	0.27	0.44	5.8	40	0.05
para_k2	$2\sqrt{2}$	1/4	4.8	1.4	0.48	0.52	0.17	3.75	200	0.17
para_k2	$2\sqrt{2}$	1/4	9.6	0.7	0.31	0.52	0.30	—	50	0.10
para_k4	$4\sqrt{2}$	1/4	4.8	0.7	0.31	0.58	0.13	4.75	60	0.09
para_k4	$4\sqrt{2}$	1/4	9.6	0.4	0.19	0.63	0.24	—	30	0.05
para_k8	$8\sqrt{2}$	1/4	4.8	0.4	0.19	0.64	0.15	—	30	0.03
2D large, $N_x = 6912$										
para_k1	$\sqrt{2}$	1/4	2.4	11.2	0.88	0.26	0.18	2.4	1490	0.56
para_k2	$2\sqrt{2}$	1/4	2.4	5.6	0.78	0.53	0.10	2.95	1620	0.40
para_k4	$4\sqrt{2}$	1/4	2.4	2.8	0.65	0.60	0.07	3.3	510	0.26
para_k8	$8\sqrt{2}$	1/4	2.4	1.4	0.48	0.61	0.05	3.85	170	0.12
3D, $N_x = 1152$										
diag_k2	2	1/5	1.28	3.6	0.71	0.50	0.22	3.2	180	0.25
diag_k4	4	1/5	1.28	1.8	0.54	0.75	0.17	4.0	110	0.10

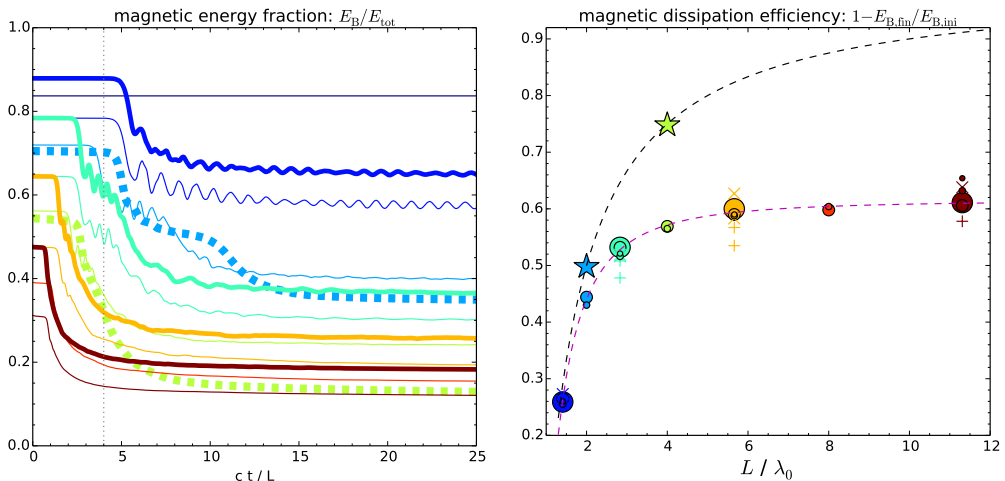


FIGURE 2. *Left panel:* time evolution of the magnetic energy \mathcal{E}_B as fraction of the total energy \mathcal{E}_{tot} for the medium (thin solid lines) and large (thick solid lines) simulation sizes. The thick dashed lines indicate two 3D simulations. The line colour indicates the effective wavenumber L/λ_0 , as shown in the right panel. *Right panel:* final magnetic dissipation efficiency $\epsilon_{\text{diss,fin}} = 1 - \mathcal{E}_{B,\text{fin}}/\mathcal{E}_{B,\text{ini}}$ (evaluated at $20 < ct/L < 25$) as function of the effective wavenumber of initial magnetic configuration L/λ_0 . The large/medium/small circles indicate new results obtained from large/medium/small simulations, the ‘+’ symbols indicate simulations for non-standard values of \tilde{a}_1 , the ‘x’ symbols indicate simulations for non-standard values of $\rho_0/\Delta x$, and the stars indicate 3D simulations. The symbol colours indicate the effective wavenumber L/λ_0 . The black dashed line shows a $1 - \lambda_0/L$ relation predicted by the relaxation theorem of Taylor (1974) and matching the 3D results, and the magenta dashed line shows a $0.62 - 0.70(\lambda_0/L)^2$ relation fitted to the 2D results.

3.2. Total energy transformations

The initial configurations investigated here involve various levels of magnetic energy $\mathcal{E}_{B,\text{ini}}$ as fractions of the total energy \mathcal{E}_{tot} . The initial magnetic energy fraction decreases with increasing L/λ_0 and increases with the system size. Our simulations probe the range of $\mathcal{E}_{B,\text{ini}}/\mathcal{E}_{\text{tot}}$ values from 0.19 to 0.88. Related to the initial magnetic energy fraction is the initial mean hot magnetisation $\langle \sigma_{\text{ini}} \rangle$ (see Eq. 2.9), which in our simulations takes values from 0.35 to 11.2.

Time evolutions of the magnetic energy fractions are presented in the left panel of Figure 2. In all studied cases, the magnetic energy experiences a sudden decrease followed by a slow settling. As the settling is largely complete by $t = 20L/c$, we measure the final magnetic energy fraction $\mathcal{E}_{B,\text{fin}}$ as the average over the $20 < ct/L < 25$ period. We define the final magnetic dissipation efficiency as $\epsilon_{\text{diss,fin}} = 1 - \mathcal{E}_{B,\text{fin}}/\mathcal{E}_{B,\text{ini}}$. The right panel of Figure 2 shows that $\epsilon_{\text{diss,fin}}$ is a function of magnetic topology parameter L/λ_0 , almost independent of the system size L (although it is slightly lower for reduced values of \tilde{a}_1). For large values of L/λ_0 , magnetic dissipation efficiency appears to saturate at the level of $\epsilon_{\text{diss}} \sim 0.6$. We have fitted the large and medium 2D results for the standard values of \tilde{a}_1 and $\rho_0/\Delta x$ with a relation $\epsilon_{\text{diss}} = \epsilon_0 - \epsilon_2(\lambda_0/L)^2$, finding $\epsilon_0 \simeq 0.62$ and $\epsilon_2 \simeq 0.70$.

Also shown in Figure 2 are analogous results for two 3D simulations. These results are consistent with a relation $\epsilon_{\text{diss}} = 1 - \lambda_0/L$ predicted by the relaxation theorem of Taylor (1974).

The initial sudden decrease of the magnetic energy is mediated by rapid growth of the electric energy. Time evolutions of the electric energy \mathcal{E}_E as fraction of the initial

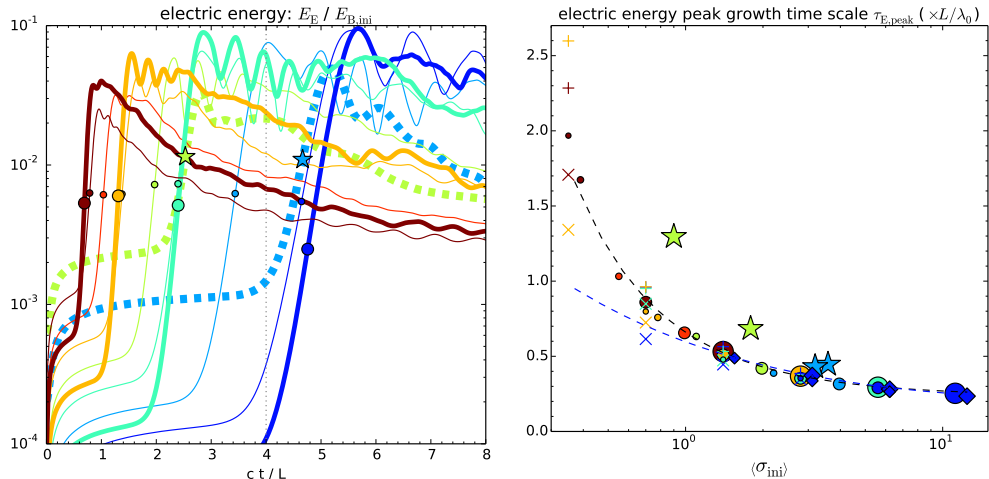


FIGURE 3. *Left panel:* time evolution of the electric energy \mathcal{E}_E as fraction of the initial magnetic energy $\mathcal{E}_{B,ini}$. The line types are the same as in the left panel of Figure 2. Moments of minimum growth time scale are indicated with the filled symbols. *Right panel:* minimum growth time scales for the total electric energy τ_E as function of the initial mean magnetisation $\langle \sigma_{ini} \rangle$. The symbol types are the same as in the right panel of Figure 2; in addition the blue diamonds indicate the `para_k1` simulations from Nalewajko *et al.* (2016), and original shorter 3D runs from Nalewajko (2018) are indicated. The black dashed line shows a β_A^{-3} trend (see Eq. 3.1) fitted to all 2D results. The blue dashed line shows a different trend (see Eq. 4.1) suggested previously by Nalewajko *et al.* (2016).

magnetic energy $\mathcal{E}_{B,ini}$ are presented in the left panel of Figure 3. In all studied cases we find an episode of rapid exponential growth of the electric energy, an indication of linear instability known as coalescence instability (East *et al.* 2015). We indicate moments of peak electric energy growth time scale $\tau_{E,peak}$ (defined by $\mathcal{E}_E \propto \exp(ct/L\tau_E)$). The right panel of Figure 3 compares the values of $\tau_{E,peak}$, multiplied by L/λ_0 , as function of the initial mean magnetisation $\langle \sigma_{ini} \rangle$. Combining our 2D results with the previous simulations for the case `para_k1` reported in Nalewajko *et al.* (2016), the relation between $\tau_{E,peak}$ and $\langle \sigma_{ini} \rangle$ for the standard values of \tilde{a}_1 and $\rho_0/\Delta x$ has been fitted as:

$$\tau_{E,peak} \simeq \frac{0.233 \pm 0.005}{(L/\lambda_0)\beta_{A,ini}^3}, \quad (3.1)$$

where $\beta_{A,ini} = [\langle \sigma_{ini} \rangle / (1 + \langle \sigma_{ini} \rangle)]^{1/2}$ is the characteristic value of initial Alfvén velocity. The four 3D simulations (including two new full runs and two shorter runs from Nalewajko 2018) show longer growth time scales compared with their 2D counterparts, with the cases `para_k4` being strongly affected by the noise component of the electric field.

3.3. Conservation of total energy and magnetic helicity

Figure 4 shows the conservation accuracy for the total system energy \mathcal{E}_{tot} and total magnetic helicity $\mathcal{H} = \int H dV$ (where $H = \mathbf{A} \cdot \mathbf{B}$ with \mathbf{A} the magnetic vector potential). The conservation accuracy for parameter X is defined as $\delta_X \equiv \max |X(ct < 25L)/X(t = 0) - 1|$. The conservation accuracy of total energy $\delta_{\mathcal{E}}$ is presented as function of modified magnetisation parameter $\sigma_{\mathcal{E}} \equiv \langle \sigma_{ini} \rangle (2.4\Delta x/\rho_0)^{-3/4} (L/2880\rho_0)^{-3/4}$. For $1 < \sigma_{\mathcal{E}} < 6$ (essentially for $L/\lambda_0 \gtrsim 2\sqrt{2}$), energy conservation accuracy scales like $\delta_{\mathcal{E}} \propto \sigma_{\mathcal{E}}^{-5/2} \propto \langle \sigma_{ini} \rangle^{-5/2} (\Delta x/\rho_0)^{15/8 \approx 2} (L/\rho_0)^{15/8 \approx 2}$, reaching the value of $\simeq 0.02$ for $\sigma_{\mathcal{E}} \simeq 1$. For $\sigma_{\mathcal{E}} >$

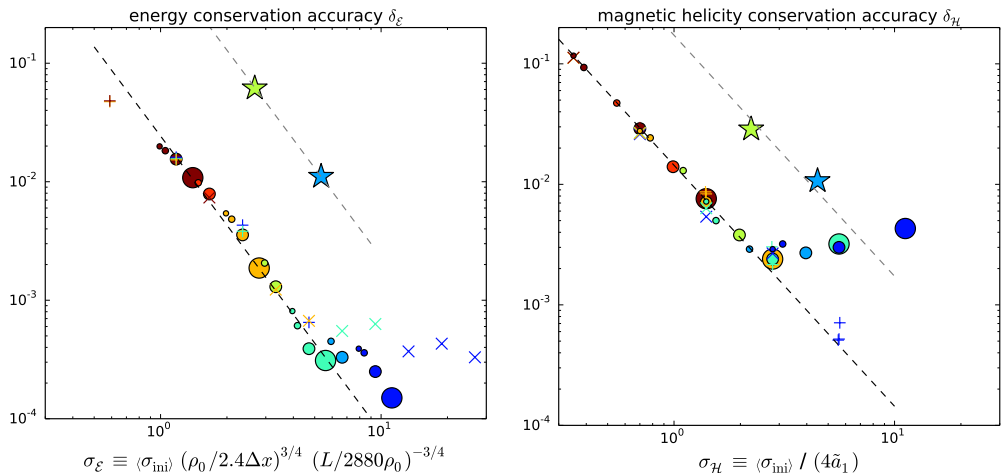


FIGURE 4. Conservation accuracies of total energy $\delta_{\mathcal{E}}$ (*left panel*) and total magnetic helicity $\delta_{\mathcal{H}}$ (*right panel*) as functions of modified magnetisation parameters $\sigma_{\mathcal{E}}$ and $\sigma_{\mathcal{H}}$, respectively, chosen to minimise scatter around the suggested trends (dashed lines; $\sigma_{\mathcal{E}}^{-5/2}$ and $\sigma_{\mathcal{H}}^{-2}$, respectively), see the main text for details. The symbol types are the same as in the right panel of Figure 2.

6, energy conservation accuracy is found to be of the order $\delta_{\mathcal{E}} \sim 3 \times 10^{-4}$. In the 3D cases, energy conservation is found to be worse by factor $\simeq 30$ as compared with the 2D results for the same value of $\sigma_{\mathcal{E}}$.

The conservation accuracy of total magnetic helicity $\delta_{\mathcal{H}}$ is presented as function of a different modified magnetisation parameter $\sigma_{\mathcal{H}} \equiv \langle \sigma_{\text{ini}} \rangle / (4 \tilde{a}_1) \simeq \lambda_0 / 182 \rho_0$ (the latter assuming $\Theta = 1$). For $\sigma_{\mathcal{H}} < 2.5$, magnetic helicity conservation accuracy scales like $\delta_{\mathcal{H}} \propto \sigma_{\mathcal{H}}^{-2} \propto (\lambda_0 / \rho_0)^{-2}$, reaching the value of $\simeq 0.1$ for $\sigma_{\mathcal{H}} \simeq 0.4$. For $\sigma_{\mathcal{H}} > 2.5$ (essentially for $L / \lambda_0 \lesssim 2$), we find that simulations with reduced values of \tilde{a}_1 appear to follow the same trend, however large and medium simulations with standard \tilde{a}_1 value show worse conservation of the order $\delta_{\mathcal{H}} \sim 3 \times 10^{-3}$. In the 3D cases, magnetic helicity conservation is found to be worse by factor ~ 12 as compared with the 2D results for the same value of $\sigma_{\mathcal{H}}$.

3.4. Particle energy distributions

Figure 5 shows the particle momentum distributions $N(u)$ (closely related to the energy distributions for $u = \sqrt{\gamma^2 - 1} \gg 1$) for the final states of the medium and large 2D simulations, as well as the 3D simulations (averaged over the time range of $20 < ct/L < 25$). The non-evolving case `diag_k1` is equivalent to the initial Maxwell-Jüttner distribution. A high-energy excess is evident in all other cases.

There are several ways to characterise this excess component. In most cases, a power-law section can be clearly identified. Accurate evaluation of the corresponding power-law index p (such that $N(u) \propto u^{-p}$) is in general complicated, as it requires fitting analytical functions that properly represent the high-energy cutoff (Werner *et al.* 2016). Here, in order to avoid those complications, we estimate a power-law index using a compensation method, multiplying the measured distribution by u^p with different p values to obtain the broadest and most balanced plateau section. The accuracy of this method is estimated at ± 0.05 . The best values of p estimated for our simulations are reported in Table 1. No power-law sections could be identified for certain cases with low initial magnetisations

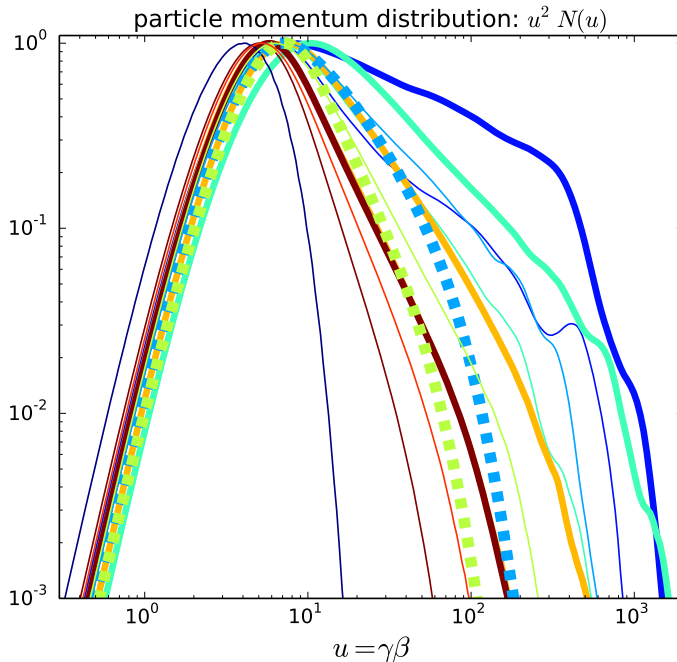


FIGURE 5. Momentum distributions $u^2 N(u)$ of electrons and positrons averaged over the time period $20 < ct/L < 25$. The line types are the same as in the left panel of Figure 2.

$\langle \sigma_{\text{ini}} \rangle < 1$. The hardest spectrum with $p \simeq 2.4$ has been found for the large simulation **para_k1**. A similar spectrum with $p \simeq 2.45$ (reexamined with the same method) has been obtained in previous simulations for the case **para_k1** reported in Nalewajko *et al.* (2016) and characterised by slightly higher initial magnetisation of $\langle \sigma_{\text{ini}} \rangle = 12.4$.

The left panel of Figure 6 shows the power-law index p as function of the initial magnetic energy fraction $\mathcal{E}_{\text{B,ini}}/\mathcal{E}_{\text{tot}}$. The value of p is strongly anti-correlated with $\mathcal{E}_{\text{B,ini}}/\mathcal{E}_{\text{tot}}$, independent of the simulation size, with the Pearson correlation coefficient of $\simeq -0.98$. A linear trend has been fitted to the results of 2D simulations with standard values of \tilde{a}_1 and $\rho_0/\Delta x$, including the previous **para_k1** simulations from Nalewajko *et al.* (2016):

$$p \simeq (-3.9 \pm 0.2) \frac{\mathcal{E}_{\text{B,ini}}}{\mathcal{E}_{\text{tot}}} + (5.8 \pm 0.1). \quad (3.2)$$

Also shown are results for two 3D simulations showing particle distributions slightly steeper as compared with 2D simulations with comparable initial magnetic energy fractions.

The high-momentum excess component of the particle distribution can be alternatively characterised by the maximum particle energy reached γ_{max} . Here, the value of γ_{max} is evaluated at the fixed level of 10^{-3} of the $u^2 N(u)$ distribution normalised to peak at unity (cf. the bottom edge of Figure 5). The final values of γ_{max} for our large simulations are reported in Table 1. The highest value of $\gamma_{\text{max}} \simeq 1620$ has been found for the large simulation **para_k2**. For the cases where the power-law index p could be evaluated (note that γ_{max} can always be evaluated), $\log \gamma_{\text{max}}$ is strongly anti-correlated with p , with the Pearson correlation coefficient of $\simeq -0.99$.

Yet another approach to the high-momentum excess is to fit and subtract a low-

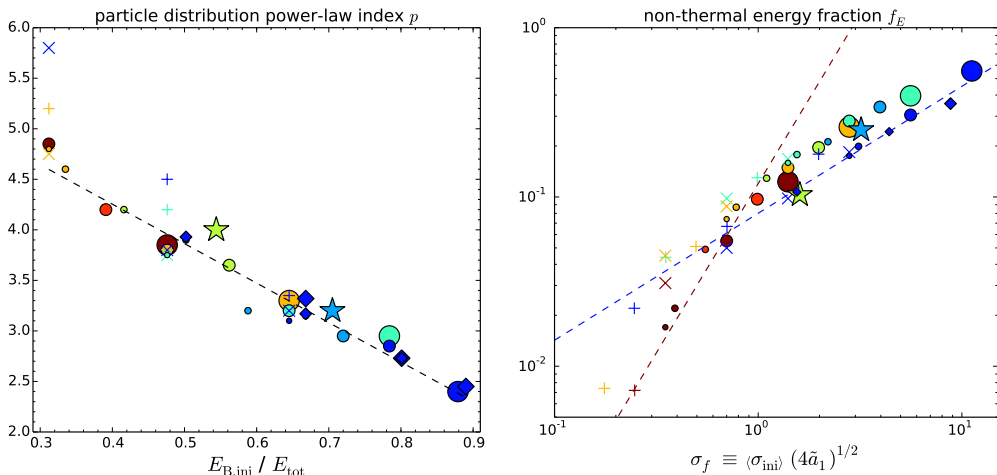


FIGURE 6. *Left panel:* power-law index p of the momentum distribution $N(u) \propto u^{-p}$ as function of the initial magnetic energy fraction $\mathcal{E}_{B,ini}/\mathcal{E}_{tot}$. The black dashed line shows a linear trend fitted to all 2D results. *Right panel:* non-thermal energy fraction f_E as function of a modified magnetisation parameter σ_f . The dashed lines indicate two trends: $\propto \sigma_f^{3/4}$ (blue) and $\propto \sigma_f^2$ (brown). For both panels, the symbol types are the same as in the right panel of Figure 3.

momentum Maxwell-Jüttner component and to calculate the non-thermal fractions of particle number f_n and particle energy f_E contained in the remaining excess. This fitting was performed using the weighted least squares method with the weights proportional to u^{-2} . In all cases, the non-thermal number fractions were found to be closely related to the energy fractions as $f_n \simeq f_E/3.5$. The values of non-thermal energy fractions f_E for our simulations are reported in Table 1. The highest value of $f_E \simeq 56\%$ has been found for the large simulation `diag_k1`. For the cases where p could be evaluated, f_E is anti-correlated with p , with the Pearson correlation coefficient of $\simeq -0.93$.

The right panel of Figure 6 shows the non-thermal energy fraction f_E vs. another modified magnetisation parameter $\sigma_f \equiv \langle \sigma_{ini} \rangle (4\tilde{a}_1)^{1/2}$. We also indicate the $f_E \propto \langle \sigma_{ini} \rangle^{3/4}$ trend suggested by Nalewajko *et al.* (2016) and re-fitted only to the `para_k1` results (deep blue symbols). We confirm that this trend describes the `para_k1` results reasonably well, however, it is not followed by the high- (L/λ_0) cases that probe lower magnetisation values $\sigma_f < 1$. In the particular case of $L/\lambda_0 = 8\sqrt{2}$ (brown symbols), the values of f_E decrease faster with decreasing σ_f , roughly like $f_E \propto \sigma_f^2$ for $\sigma_f < 1$. For intermediate magnetisation values $1 < \sigma_f < 10$, the values of f_E for $L/\lambda_0 > \sqrt{2}$ are systematically higher as compared with the `para_k1` trend line. The 3D simulations produced f_E values that are consistent (in the case `diag_k2`) or somewhat lower (in the case `diag_k4`) than the 2D results.

We use the final non-thermal energy fractions f_E to divide the global energy gain of the particles into the non-thermal and thermal parts:

$$\Delta\mathcal{E}_{nth} = f_E \mathcal{E}_{kin,fin}, \quad (3.3)$$

$$\Delta\mathcal{E}_{th} = (1 - f_E)\mathcal{E}_{kin,fin} - \mathcal{E}_{kin,ini}, \quad (3.4)$$

where $\mathcal{E}_{kin,ini} = \mathcal{E}_{tot} - \mathcal{E}_{B,ini}$ and $\mathcal{E}_{kin,fin} \simeq \mathcal{E}_{tot} - \mathcal{E}_{B,fin}$, since by $ct = 25L$ the total electric energy that mediates the dissipation of magnetic energy decreases to the level of $\mathcal{E}_{E,fin} < 10^{-2}\mathcal{E}_{tot}$. The two components of particle energy

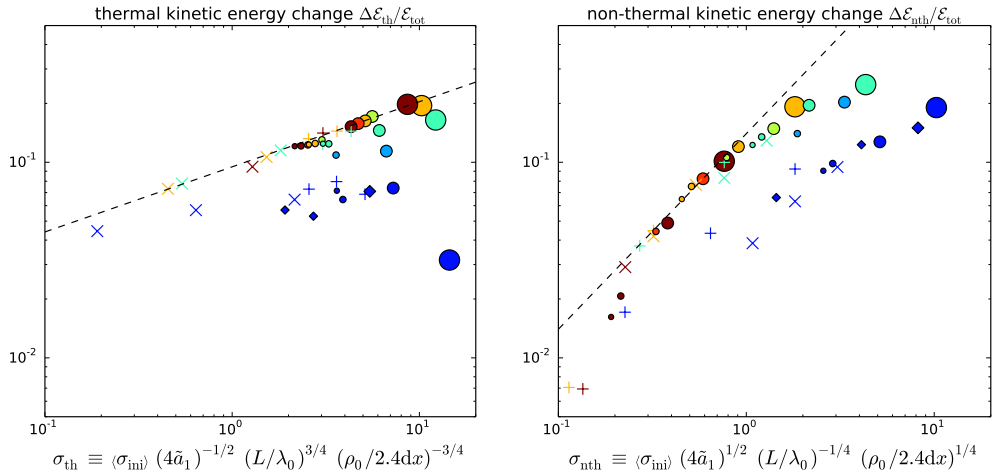


FIGURE 7. Global gain of the particle energy divided into thermal $\Delta\mathcal{E}_{\text{th}}$ (left panel) and non-thermal $\Delta\mathcal{E}_{\text{nth}}$ (right panel) components, normalised to the total energy \mathcal{E}_{tot} , as functions of modified magnetisation parameters σ_{th} and σ_{nth} , respectively, chosen to minimise scatter around suggested trends (dashed black lines) $\propto \sigma_{\text{th}}^{1/3}$ and $\propto \sigma_{\text{nth}}$, respectively. The symbol types are the same as in the right panel of Figure 3.

gain are presented in Figure 7 as functions of yet two other modified magnetisation parameters $\sigma_{\text{th}} \equiv \langle\sigma_{\text{ini}}\rangle (4\tilde{a}_1)^{-1/2} (L/\lambda_0)^{3/4} (2.4\Delta x/\rho_0)^{3/4}$ and $\sigma_{\text{nth}} \equiv \langle\sigma_{\text{ini}}\rangle (4\tilde{a}_1)^{1/2} (L/\lambda_0)^{-1/4} (2.4\Delta x/\rho_0)^{-1/4}$, respectively. We find that the cases of `para_k1` (deep blue symbols) stand out from other cases, having significantly lower thermal energy gains, suggesting that they are limited by the magnetic topology. On the other hand, their non-thermal energy gains are comparable to other cases, but achieved at significantly higher values of σ_{nth} . Power-law trends can be suggested only for sufficiently high wavenumbers ($L/\lambda_0 \gtrsim 4\sqrt{2}$): $\Delta\mathcal{E}_{\text{th}} \propto \sigma_{\text{th}}^{1/3}$ and $\Delta\mathcal{E}_{\text{nth}} \propto \sigma_{\text{nth}}$, respectively. However, in the `diag_k8` cases (brown symbols), a steeper trend for the non-thermal energy gain $\Delta\mathcal{E}_{\text{nth}} \propto \sigma_{\text{nth}}^{5/2}$ is apparent for low magnetisation values $\sigma_{\text{nth}} < 0.25$. The highest value of $\Delta\mathcal{E}_{\text{nth}}/\mathcal{E}_{\text{tot}} \simeq 25\%$ is obtained for our large simulation `diag_k2`.

4. Discussion

Our new results extend the previous study of 2D PIC simulations of ABC fields for the `para_k1` case in the non-radiative regime (Nalewajko *et al.* 2016), and connect it with a study of 3D PIC simulations for the cases `diag_k2` and `diag_k4` (Nalewajko 2018). They can also be compared with the FF simulations of ABC fields presented in Zrake & East (2016). In particular, the magnetic dissipation efficiency in the FF limit in 2D has been estimated at $\epsilon_{\text{diss}} \simeq 70\%$, while our results suggest $\epsilon_{\text{diss}} \simeq 62\%$ in the limit of $L/\lambda_0 \gg 1$. It should be noted, however, that in PIC simulations this limit forces us towards lower magnetisation values.

In Nalewajko *et al.* (2016), a relation between the electric energy growth time scale $\tau_{\text{E,peak}}$ and the initial characteristic hot magnetisation σ_{hot} was suggested in the following form:

$$\tau_{\text{E,peak}} \simeq \frac{0.13}{v_A(0.21\sigma_{\text{hot}})}, \quad (4.1)$$

where $v_A(\sigma) \equiv [\sigma/(1 + \sigma)]^{1/2}$ was treated as a function in the form of Alfvén velocity of arbitrarily scaled argument σ , and $\sigma_{\text{hot}} \equiv \langle \sigma_{\text{ini}} \rangle / 2$ was a characteristic value of hot magnetisation based on B_0^2 instead of the mean value $\langle B^2 \rangle$ used here†. The above relation is shown in the right panel of Figure 3 with a dashed blue line (cf. Figure 3 of Nalewajko *et al.* 2016). We can see that the previously suggested trend agrees very well with the previous measurements from Nalewajko *et al.* (2016), and is very close to the new trend line in the range of $1.5 < \langle \sigma_{\text{ini}} \rangle < 12.5$. However, the previous trend predicts significantly shorter growth time scales for low magnetisation values $\langle \sigma_{\text{ini}} \rangle < 1$ that is probed here with simulations for $L/\lambda_0 \geq 4\sqrt{2}$.

Our new scaling described by Eq. (3.1) is more natural, without arbitrary scaling parameters. It suggests that in the FF limit, when $\langle \sigma_{\text{ini}} \rangle \rightarrow \infty$ and $\beta_{\text{A,ini}} \rightarrow 1$, we should expect that the growth time scale should become $\tau_{\text{E,FF}} \simeq 0.233/(L/\lambda_0)$. For $L/\lambda_0 = \sqrt{2}$, this would yield $\tau_{\text{E,FF}} \simeq 0.16$, somewhat longer than $\tau_{\text{E,FF}} \simeq 0.13$ indicated by Nalewajko *et al.* (2016). As for why should $\tau_{\text{E,peak}}(L/\lambda_0)$ scale with $\beta_{\text{A,ini}}^{-3}$ requires a theoretical investigation of the linear coalescence instability beyond the FF limit, with proper treatment of magnetic nulls, which is beyond the scope of this work.

We can only partially confirm a relation between non-thermal energy fraction and initial mean hot magnetisation $f_E \propto \langle \sigma_{\text{ini}} \rangle^{3/4}$ originally suggested in Nalewajko *et al.* (2016). This relation appears to hold for the `para_k1` case, including new simulations extending into the $\langle \sigma_{\text{ini}} \rangle \sim 1$ regime, and possibly also for higher values of L/λ_0 as long as $\sigma_f > 1$ (see the right panel of Figure 6). However, for the cases where a power-law index p can be determined, a simple linear relation holds between p and the initial magnetic energy fraction $\mathcal{E}_{\text{B,ini}}/\mathcal{E}_{\text{tot}}$ (see Eq. 3.2), at least over the studied range of $0.3 < \mathcal{E}_{\text{B,ini}}/\mathcal{E}_{\text{tot}} < 0.9$ (see the left panel of Figure 6).

We have introduced several *modified magnetisation* parameters, as combinations of the initial mean magnetisation $\langle \sigma_{\text{ini}} \rangle$ with other input parameters, in order to describe the scalings of global output parameters. The particular formulae for the modified magnetisations were chosen in order to minimise scatter around the suggested trends, with the exponents of $\Delta x/\rho_0$, L/ρ_0 , L/λ_0 and \tilde{a}_1 estimated empirically with the accuracy of $\sim \pm 1/4$. The energy conservation accuracy for ABC fields simulated with the `Zeltron` code is found to scale roughly like $\delta_{\mathcal{E}} \propto \langle \sigma_{\text{ini}} \rangle^{-5/2} (\Delta x/\rho_0)^2 (L/\rho_0)^2$, not sensitive to λ_0 . This is different from the reference case of uniform magnetic field, in which we found $\delta_{\mathcal{E}} \propto \langle \sigma_{\text{ini}} \rangle^{-1} (\Delta x/\rho_0)^2$, independent of L . On the other hand, the magnetic helicity conservation accuracy is found to scale like $\delta_{\mathcal{H}} \propto (\lambda_0/\rho_0)^{-2}$, but it is not sensitive to $\Delta x/\rho_0$ or L/ρ_0 . This is in contrast to the force-free simulations of Zrake & East (2016), in which $\delta_{\mathcal{H}} \propto (\Delta x)^{2.8}$. Further investigation is required in order to explain these differences.

For the non-thermal energy fraction f_E , the scaling with initial mean magnetisation $\langle \sigma_{\text{ini}} \rangle$ is rather ambiguous. Only in the special case of $L/\lambda_0 = \sqrt{2}$ we have sufficient range of $\langle \sigma_{\text{ini}} \rangle$ values to claim that $f_E \propto \langle \sigma_{\text{ini}} \rangle^{3/4}$; this scaling is improved by additional dependence on the particle anisotropy level \tilde{a}_1 . The scalings of thermal and non-thermal kinetic energy gains, $\Delta \mathcal{E}_{\text{th}}$ and $\Delta \mathcal{E}_{\text{nth}}$, respectively, can in principle be derived from the scalings of f_E and magnetic dissipation efficiency ϵ_{diss} . The ambiguity of the f_E scaling makes it not straightforward to predict in detail the scalings of $\Delta \mathcal{E}_{\text{th}}$ and $\Delta \mathcal{E}_{\text{nth}}$.

The initial mean hot magnetisation $\langle \sigma_{\text{ini}} \rangle$ of ABC fields with relativistically warm plasma ($\Theta = 1$) is strongly limited by the simulation size, especially if one would like to resolve numerically all the fundamental length scales, in particular the nominal gyroradius ρ_0 . For a given effective wavenumber L/λ_0 , higher values of $\langle \sigma_{\text{ini}} \rangle$ can only be

† We note that the characteristic values of σ_{hot} reported in Nalewajko *et al.* (2016) were underestimated by a constant factor of $\simeq 1.13$.

reached by increasing the system size L/ρ_0 ‡. It can be expected that larger simulations would show more effective non-thermal particle acceleration with harder high-energy tails indicated by higher values of non-thermal energy fractions f_e and lower values of power-law indices p . Eventually, at sufficiently high $\langle\sigma_{\text{ini}}\rangle$, and with $L/\lambda_0 \geq 2$, it should be possible to achieve particle distributions dominated energetically by the high-energy particles, with $p < 2$, as has been demonstrated in the case of Harris-layer reconnection (Sironi & Spitkovsky 2014; Guo *et al.* 2014; Werner *et al.* 2016; Kagan *et al.* 2018). What remains unclear, though, is the level of thermal energy gains.

Our results show that the case `para.k1` characterised by the lowest unstable effective wavenumber $L/\lambda_0 = \sqrt{2}$, studied in detail by Nalewajko *et al.* (2016) and Yuan *et al.* (2016), has a limited efficiency of both thermal and non-thermal particle acceleration, which is related to the limited magnetic dissipation efficiency. On the other hand, 2D ABC fields with high L/λ_0 values, although also limited by topological constraints (Zrake & East 2016), can be used as a model for kinetic investigations of decaying relativistic magnetised turbulence, an alternative to uncorrelated magnetic fluctuations (Comisso & Sironi 2018, 2019; Comisso *et al.* 2020). Relativistic magnetised turbulence has also been investigated extensively by means of PIC simulations in the driven mode (Zhdankin *et al.* 2017*b,a*, 2018, 2019, 2020; Wong *et al.* 2020).

These results are based on numerical simulations performed at the supercomputer `Prometheus` located at the Academic Computer Centre ‘Cyfronet’ of the AGH University of Science and Technology in Krakow, Poland (PLGrid grants `plgpic20`, `ehtsim`); and at the computing cluster `Chuck` located at the Nicolaus Copernicus Astronomical Center of the Polish Academy of Sciences in Warsaw, Poland. QC and KN were supported by the Polish National Science Center grant 2015/18/E/ST9/00580. BM acknowledges support from DOE through the LDRD program at LANL and NASA Astrophysics Theory Program.

REFERENCES

- ABDO, A. A., ET AL. 2011*a* Gamma-ray flares from the Crab Nebula. *Science* **331** (6018), 739–742.
- ABDO, A. A., ET AL. 2011*b* Fermi Gamma-ray Space Telescope observations of the gamma-ray outburst from 3C454.3 in November 2010. *Astrophys. J.* **733** (2), L26.
- ACKERMANN, M., ET AL. 2016 Minute-timescale > 100 MeV γ -ray variability during the giant outburst of quasar 3C 279 observed by Fermi-LAT in 2015 June. *Astrophys. J.* **824** (2), L20.
- AHARONIAN, F., ET AL. 2007 An exceptional very high energy gamma-ray flare of PKS 2155-304. *Astrophys. J.* **664** (2), L71–L74.
- ALBERT, J., ET AL. 2007 Variable very high energy gamma-ray emission from Markarian 501. *Astrophys. J.* **669** (2), 862–883.
- ALEKSIĆ, J., ET AL. 2011 Magic discovery of very high energy emission from the FSRQ PKS 1222+21. *Astrophys. J.* **730** (1), L8.
- ARNOLD, V. 1965 Sur une proprietes topologique des applications globalment canonique de la mecanique classique. *CR. Acad. Sci. Paris* **261**, 3719-3722.
- ARONS, J. 2012 Pulsar wind nebulae as cosmic pevatrons: A current sheet’s tale. *Space Sci. Rev.* **173** (1-4), 341–367.
- BESSHO, N. & BHATTACHARJEE, A. 2012 Fast magnetic reconnection and particle acceleration in relativistic low-density electron-positron plasmas without guide field. *Astrophys. J.* **750** (2), 129.

‡ One can achieve a somewhat higher $\langle\sigma_{\text{ini}}\rangle$ by increasing the local particle anisotropic parameter \tilde{a}_1 . However, some numerical artefacts are observed for $\tilde{a}_1 \simeq 1/2$.

- BLANDFORD, R., YUAN, Y., HOSHINO, M. & SIRONI, L. 2017 Magnetoluminescence. *Space Sci. Rev.* **207** (1-4), 291–317.
- BUEHLER, R., ET AL. 2012 Gamma-ray activity in the Crab Nebula: the exceptional flare of 2011 April. *Astrophys. J.* **749** (1), 26.
- BUEHLER, R. & BLANDFORD, R. 2014 The surprising Crab pulsar and its nebula: a review. *Rep. Prog. Phys.* **77** (6), 066901.
- CERUTTI, B., WERNER, G. R., UZDENSKY, D. A. & BEGELMAN, M. C. 2012 Beaming and rapid variability of high-energy radiation from relativistic pair plasma reconnection. *Astrophys. J.* **754** (2), L33.
- CERUTTI, B., WERNER, G. R., UZDENSKY, D. A. & BEGELMAN, M. C. 2013 Simulations of particle acceleration beyond the classical synchrotron burnoff limit in magnetic reconnection: An explanation of the Crab flares. *Astrophys. J.* **770** (2), 147.
- CERUTTI, B., WERNER, G. R., UZDENSKY, D. A. & BEGELMAN, M. C. 2014 Three-dimensional relativistic pair plasma reconnection with radiative feedback in the Crab Nebula. *Astrophys. J.* **782** (2), 104.
- CHRISTIE, I. M., PETROPOULOU, M., SIRONI, L. & GIANNIOS, D. 2018 Radiative signatures of plasmoid-dominated reconnection in blazar jets. *Mon. Not. R. Astron. Soc.* **482** (1), 65–82.
- CLAUSEN-BROWN, E. & LYUTIKOV, M. 2012 Crab Nebula gamma-ray flares as relativistic reconnection minijets. *Mon. Not. R. Astron. Soc.* **426** (2), 1374–1384.
- COMISSO, L. & SIRONI, L. 2018 Particle acceleration in relativistic plasma turbulence. *Phys. Rev. Lett.* **121**, 255101.
- COMISSO, L. & SIRONI, L. 2019 The interplay of magnetically dominated turbulence and magnetic reconnection in producing nonthermal particles. *Astrophys. J.* **886** (2), 122.
- COMISSO, L., SOBACCHI, E. & SIRONI, L. 2020 Hard synchrotron spectra from magnetically dominated plasma turbulence. *Astrophys. J.* **895** (2), L40.
- EAST, W. E., ZRAKE, J., YUAN, Y. & BLANDFORD, R. D. 2015 Spontaneous decay of periodic magnetostatic equilibria. *Phys. Rev. Lett.* **115**, 095002.
- GIANNIOS, D. 2013 Reconnection-driven plasmoids in blazars: fast flares on a slow envelope. *Mon. Not. R. Astron. Soc.* **431** (1), 355–363.
- GIANNIOS, D., UZDENSKY, D. A. & BEGELMAN, M. C. 2009 Fast TeV variability in blazars: jets in a jet. *Mon. Not. R. Astron. Soc.* **395** (1), L29–L33.
- GUO, F., LI, H., DAUGHTON, W. & LIU, Y.-H. 2014 Formation of hard power laws in the energetic particle spectra resulting from relativistic magnetic reconnection. *Phys. Rev. Lett.* **113**, 155005.
- GUO, F., LI, X., DAUGHTON, W., KILIAN, P., LI, H., LIU, Y.-H., YAN, W. & MA, D. 2019 Determining the dominant acceleration mechanism during relativistic magnetic reconnection in large-scale systems. *Astrophys. J.* **879** (2), L23.
- GUO, F., LI, X., DAUGHTON, W., LI, H., KILIAN, P., LIU, Y.-H., ZHANG, Q. & ZHANG, H. 2020 Magnetic energy release, plasma dynamics and particle acceleration during relativistic turbulent magnetic reconnection, arXiv: 2008.02743.
- GUO, F., LI, X., LI, H., DAUGHTON, W., ZHANG, B., LLOYD-RONNING, N., LIU, Y.-H., ZHANG, H. & DENG, W. 2016 Efficient production of high-energy nonthermal particles during magnetic reconnection in a magnetically dominated ion–electron plasma. *Astrophys. J.* **818** (1), L9.
- GUO, F., LIU, Y.-H., DAUGHTON, W. & LI, H. 2015 Particle acceleration and plasma dynamics during magnetic reconnection in the magnetically dominated regime. *Astrophys. J.* **806** (2), 167.
- HOSHINO, MASAHIRO 2012 Stochastic Particle Acceleration in Multiple Magnetic Islands during Reconnection. *Phys. Rev. Lett.* **108**, 135003.
- JAROSCHEK, C. H., TREUMANN, R. A., LESCH, H. & SCHOLER, M. 2004 Fast reconnection in relativistic pair plasmas: analysis of particle acceleration in self-consistent full particle simulations. *Phys. Plasmas* **11** (3), 1151–1163.
- KAGAN, D., MILOSAVLJEVIĆ, M. & SPITKOVSKY, A. 2013 A flux rope network and particle acceleration in three-dimensional relativistic magnetic reconnection. *Astrophys. J.* **774** (1), 41.

- KAGAN, D., NAKAR, E. & PIRAN, T. 2016 Beaming of particles and synchrotron radiation in relativistic magnetic reconnection. *Astrophys. J.* **826** (2), 221.
- KAGAN, D., NAKAR, E. & PIRAN, T. 2018 Physics of the saturation of particle acceleration in relativistic magnetic reconnection. *Mon. Not. R. Astron. Soc.* **476** (3), 3902–3912.
- KIRK, J. G. & SKJARAASEN, O. 2003 Dissipation in poynting-flux-dominated flows: The sigma-problem of the Crab pulsar wind. *Astrophys. J.* **591** (1), 366–379.
- KOMISSAROV, S. S. 2012 Magnetic dissipation in the Crab Nebula. *Mon. Not. R. Astron. Soc.* **428** (3), 2459–2466.
- KOMISSAROV, S. S. & LYUTIKOV, M. 2011 On the origin of variable gamma-ray emission from the Crab Nebula. *Mon. Not. R. Astron. Soc.* **414** (3), 2017–2028.
- LIU, W., LI, H., YIN, L., ALBRIGHT, B. J., BOWERS, K. J. & LIANG, E. P. 2011 Particle energization in 3D magnetic reconnection of relativistic pair plasmas. *Phys. Plasmas* **18** (5), 052105.
- LYUBARSKY, Y. & LIVERTS, M. 2008 Particle acceleration in the driven relativistic reconnection. *Astrophys. J.* **682** (2), 1436–1442.
- LYUBARSKY, Y. E. 2012 Highly magnetized region in pulsar wind nebulae and origin of the Crab gamma-ray flares. *Mon. Not. R. Astron. Soc.* **427** (2), 1497–1502.
- LYUTIKOV, M., KOMISSAROV, S., SIRONI, L. & PORTH, O. 2018 Particle acceleration in explosive relativistic reconnection events and Crab Nebula gamma-ray flares. *J. Plasma Phys.* **84** (2), 635840201.
- LYUTIKOV, M., SIRONI, L., KOMISSAROV, S. S. & PORTH, O. 2017a Explosive x-point collapse in relativistic magnetically dominated plasma. *J. Plasma Phys.* **83** (6), 635830601.
- LYUTIKOV, M., SIRONI, L., KOMISSAROV, S. S. & PORTH, O. 2017b Particle acceleration in relativistic magnetic flux-merging events. *J. Plasma Phys.* **83** (6), 635830602.
- MAYER, M., BUEHLER, R., HAYS, E., CHEUNG, C. C., DUTKA, M. S., GROVE, J. E., KERR, M. & OJHA, R. 2013 Rapid gamma-ray flux variability during the 2013 March Crab Nebula flare. *Astrophys. J.* **775** (2), L37.
- MEHLHAFF, J. M., WERNER, G. R., UZDENSKY, D. A. & BEGELMAN, M. C. 2020 Kinetic beaming in radiative relativistic magnetic reconnection: a mechanism for rapid gamma-ray flares in jets. *Mon. Not. R. Astron. Soc.* **498** (1), 799–820.
- MELZANI, MICKAËL, WALDER, ROLF, FOLINI, DORIS, WINISDOERFFER, CHRISTOPHE & FAVRE, JEAN M. 2014 The energetics of relativistic magnetic reconnection: ion-electron repartition and particle distribution hardness. *A&A* **570**, A112.
- NALEWAJKO, K. 2013 The brightest gamma-ray flares of blazars. *Mon. Not. R. Astron. Soc.* **430** (2), 1324–1333.
- NALEWAJKO, K. 2018 Relativistic magnetic reconnection in application to gamma-ray astrophysics. In *XXXVIII Polish Astronomical Society Meeting* (ed. Agata Rozanska), vol. 7, pp. 310–315, arXiv: 1808.00478.
- NALEWAJKO, K. 2018 Three-dimensional kinetic simulations of relativistic magnetostatic equilibria. *Mon. Not. R. Astron. Soc.* **481**, 4342–4354.
- NALEWAJKO, K., BEGELMAN, M. C., CERUTTI, B., UZDENSKY, D. A. & SIKORA, M. 2012 Energetic constraints on a rapid gamma-ray flare in PKS 1222+216. *Mon. Not. R. Astron. Soc.* **425** (4), 2519–2529.
- NALEWAJKO, K., GIANNIOS, D., BEGELMAN, M. C., UZDENSKY, D. A. & SIKORA, M. 2011 Radiative properties of reconnection-powered minijets in blazars. *Mon. Not. R. Astron. Soc.* **413** (1), 333–346.
- NALEWAJKO, K., YUAN, Y. & CHRUSLIŃSKA, M. 2018 Kinetic simulations of relativistic magnetic reconnection with synchrotron and inverse Compton cooling. *J. Plasma Phys.* **84** (3), 037501.
- NALEWAJKO, K., ZRAKE, J., YUAN, Y., EAST, W. E. & BLANDFORD, R. D. 2016 Kinetic simulations of the lowest-order unstable mode of relativistic magnetostatic equilibria. *Astrophys. J.* **826** (2), 115.
- ORTUÑO-MACÍAS, J. & NALEWAJKO, K. 2020 Radiative kinetic simulations of steady-state relativistic plasmoid magnetic reconnection. *Mon. Not. R. Astron. Soc.* **497** (2), 1365–1381.
- PETROPOULOU, M., GIANNIOS, D. & SIRONI, L. 2016 Blazar flares powered by plasmoids in relativistic reconnection. *Mon. Not. R. Astron. Soc.* **462** (3), 3325–3343.

- PETROPOULOU, M. & SIRONI, L. 2018 The steady growth of the high-energy spectral cut-off in relativistic magnetic reconnection. *Mon. Not. R. Astron. Soc.* **481** (4), 5687–5701.
- PETROPOULOU, M., SIRONI, L., SPITKOVSKY, A. & GIANNIOS, D. 2019 Relativistic magnetic reconnection in electron–positron–proton plasmas: Implications for jets of active galactic nuclei. *Astrophys. J.* **880** (1), 37.
- SIRONI, L., PETROPOULOU, M. & GIANNIOS, D. 2015 Relativistic jets shine through shocks or magnetic reconnection? *Mon. Not. R. Astron. Soc.* **450** (1), 183–191.
- SIRONI, L. & SPITKOVSKY, A. 2014 Relativistic reconnection: an efficient source of non-thermal particles. *Astrophys. J.* **783** (1), L21.
- STRIANI, E., ET AL. 2013 Variable gamma-ray emission from the Crab Nebula: short flares and long “waves”. *Astrophys. J.* **765** (1), 52.
- TAVANI, M., ET AL. 2011 Discovery of powerful gamma-ray flares from the Crab Nebula. *Science* **331** (6018), 736–739.
- TAYLOR, J. B. 1974 Relaxation of toroidal plasma and generation of reverse magnetic fields. *Phys. Rev. Lett.* **33**, 1139–1141.
- UZDENSKY, D. A., CERUTTI, B. & BEGELMAN, M. C. 2011 Reconnection-powered linear accelerator and gamma-ray flares in the Crab Nebula. *Astrophys. J.* **737** (2), L40.
- WERNER, G. R. & UZDENSKY, D. A. 2017 Nonthermal particle acceleration in 3D relativistic magnetic reconnection in pair plasma. *Astrophys. J.* **843** (2), L27.
- WERNER, G. R., UZDENSKY, D. A., BEGELMAN, M. C., CERUTTI, B. & NALEWAJKO, K. 2018 Non-thermal particle acceleration in collisionless relativistic electron-proton reconnection. *Mon. Not. R. Astron. Soc.* **473**, 4840–4861.
- WERNER, G. R., UZDENSKY, D. A., CERUTTI, B., NALEWAJKO, K. & BEGELMAN, M. C. 2016 The extent of power-law energy spectra in collisionless relativistic magnetic reconnection in pair plasmas. *Astrophys. J.* **816** (1), L8.
- WONG, K., ZHDANKIN, V., UZDENSKY, D. A., WERNER, G. R. & BEGELMAN, M. C. 2020 First-principles demonstration of diffusive-advective particle acceleration in kinetic simulations of relativistic plasma turbulence. *Astrophys. J.* **893** (1), L7.
- YUAN, Y., NALEWAJKO, K., ZRAKE, J., EAST, W. E. & BLANDFORD, R. D. 2016 Kinetic Study of Radiation-reaction-limited Particle Acceleration During the Relaxation of Unstable Force-free Equilibria. *Astrophys. J.* **828**, 92.
- ZENITANI, S. & HOSHINO, M. 2001 The generation of nonthermal particles in the relativistic magnetic reconnection of pair plasmas. *Astrophys. J.* **562** (1), L63–L66.
- ZENITANI, S. & HOSHINO, M. 2007 Particle acceleration and magnetic dissipation in relativistic current sheet of pair plasmas. *Astrophys. J.* **670** (1), 702–726.
- ZHDANKIN, V., UZDENSKY, D. A., WERNER, G. R. & BEGELMAN, M. C. 2017a Numerical investigation of kinetic turbulence in relativistic pair plasmas – I. Turbulence statistics. *Mon. Not. R. Astron. Soc.* **474** (2), 2514–2535.
- ZHDANKIN, V., UZDENSKY, D. A., WERNER, G. R. & BEGELMAN, M. C. 2018 System-size convergence of nonthermal particle acceleration in relativistic plasma turbulence. *Astrophys. J.* **867** (1), L18.
- ZHDANKIN, V., UZDENSKY, D. A., WERNER, G. R. & BEGELMAN, M. C. 2019 Electron and ion energization in relativistic plasma turbulence. *Phys. Rev. Lett.* **122**, 055101.
- ZHDANKIN, V., UZDENSKY, D. A., WERNER, G. R. & BEGELMAN, M. C. 2020 Kinetic turbulence in shining pair plasma: intermittent beaming and thermalization by radiative cooling. *Mon. Not. R. Astron. Soc.* **493** (1), 603–626.
- ZHDANKIN, V., WERNER, G. R., UZDENSKY, D. A. & BEGELMAN, M. C. 2017b Kinetic turbulence in relativistic plasma: From thermal bath to nonthermal continuum. *Phys. Rev. Lett.* **118**, 055103.
- ZRAKE, J. 2016 Crab flares due to turbulent dissipation of the pulsar striped wind. *Astrophys. J.* **823** (1), 39.
- ZRAKE, J. & ARONS, J. 2017 Turbulent magnetic relaxation in pulsar wind nebulae. *Astrophys. J.* **847** (1), 57.
- ZRAKE, J. & EAST, W. E. 2016 Freely decaying turbulence in force-free electrodynamics. *Astrophys. J.* **817** (2), 89.